MONASH University

PHS3350 Research Project

Crossing Relations for Double-Gluon Emission Antenna functions

Sean Solari

supervised by
Prof. Peter Skands and Christian Preuss

November 25, 2020

Contents

List of Figures

Abstract

It is known that charged particles emit radiation when they are accelerated up to high energies. This is observed in abundance from those particles accelerated within the Large-Hadron Collider, as well as from the by-products of collisions between these accelerated particles. As a consequence of this, a series of cascaded emissions or bremsstrahlung is observed in the detectors around these high-energy collisions. Due to the large number of particles involved in these so-called parton showers, direct matrix element calculations are not a viable option in trying to model these events. Instead, the known singularity structure of matrix elements in general is exploited and used to factor out a splitting function, thereby isolating the effect of individual bremsstrahlung and enabling an iterative approach to modelling parton showers.

We explore structure within the antenna function for double-gluon emission from a quark-antiquark pair in the initial state, before they annihilate to form a Z-boson. Within this antenna function, there is physically interesting structure related to the different configurations that the emitted gluons can take with respect to the quarks. Specifically, we explore the double-soft limit, wherein both gluons are emitted with negligible momenta, as well as the triple-collinear limit, where both gluons become collinear with the quark from which they were emitted. To validate the antenna function, we employ a uniform sampling over its domain and compare the resulting values to direct matrix element calculations. In a similar fashion, cuts are introduced into the domain of the antenna function to distinguish those points in phase-space corresponding to double-soft or triple-collinear configurations, thereby enabling a similar sampling of the derived limits.

Ultimately, having the structure of the antenna function in these singular limits is useful as they are likely candidates in trying to find a simple overestimate of the full matrix element to enable Monte Carlo simulations of these events. Current parton shower models view double-gluon emission as iterated single-emission, and so are not able to account for the interference effects of Feynman diagrams containing two consecutive gluon emissions. Exploring the double-gluon emission splitting function will therefore aid in understanding the role of these coherent emissions.

Acknowledgements

I would like to thank Professor Peter Skands and Christian Preuss for their supervision throughout the project, as well as Megha for her helpful discussions. Christian Preuss provided the Mathematica notebook containing the final-state A_4^0 from [5], as well as the template code as a starting point for interfacing with *Pythia 8.3*.

Introduction

The Large Hadron Collider (LHC) consists of a 27-kilometre particle beamline, to which four particle detectors are attached. The large radius of the collider is used to accelerate two beams of particles up to near the speed of light, and are shortly thereafter put on a collision course at each of these detectors. These collision events occur at extremely high energy scales, and a multitude of particles are observed within the detectors at these events, such as those within the CMS detector shown in Figure 1.1. The data from these energetic particle collisions provide an empirical source against which to compare computational predictions based on the Standard Model of particle physics in the search for new, unexplained phenomena.

However the cascade of radiation observed at these highly-energetic events remains a challenge to computationally model, due to the multitude of complex interactions that inevitably occur within these events. Specifically, we consider the collision of two beams of protons. The highly energetic partons which compose the protons in these beams are known to emit gluons through bremsstrahlung, and these gluons themselves are allowed to radiate further partons through interactions governed by Quantum Chromodynamics (QCD). Recent experiments at the LHC have used beam energies of the order teraelectron volt (TeV) and so produce an abundance of chained bremsstrahlung, resulting in a complex *parton shower*.

Due to the multitude of particles produced in these highly energetic interactions, conventional matrix element calculations from the underlying Quantum Field Theory (QFT), whose complexity is proportional to $\mathcal{O}(n!)$, are thus not a viable option in trying to model these showers. Much recent work has contributed to the development of *antenna functions*, which are mathematical objects that isolate the effect of bremsstrahlung from the initial particle collisions themselves. This is depicted graphically in Figure 2.3, wherein multiplication of the *Born-level* matrix element by the antenna function is able to reproduce those most significant effects of gluon emission.

Antenna functions therefore present as a potentially powerful tool in trying to simulate parton showers. Broadly speaking, many *parton shower algorithms* have been created to computationally model these events, and antenna functions are now being explored in part by the physics group at Monash.

Much recent effort has focussed on the use of antenna functions for single-gluon emission in parton showers, such as for the process depicted in Figure 2.3. Currently, double-gluon emissions within these parton showers are modelled through the iterative application of two single-gluon splitting functions (again similar to that of Figure 2.3). However this fails to capture some important features of coherent double-gluon emission, those emissions that can't be viewed in the iterative picture. These coherent emissions are explored in more detail throughout section 3.2.

We therefore explore antenna functions for double-gluon emission, and the singular structures contained in these double-gluon emission functions which are unique to the physical configurations that double-gluons can take, as a means to better understand double-gluon emission in parton showers.

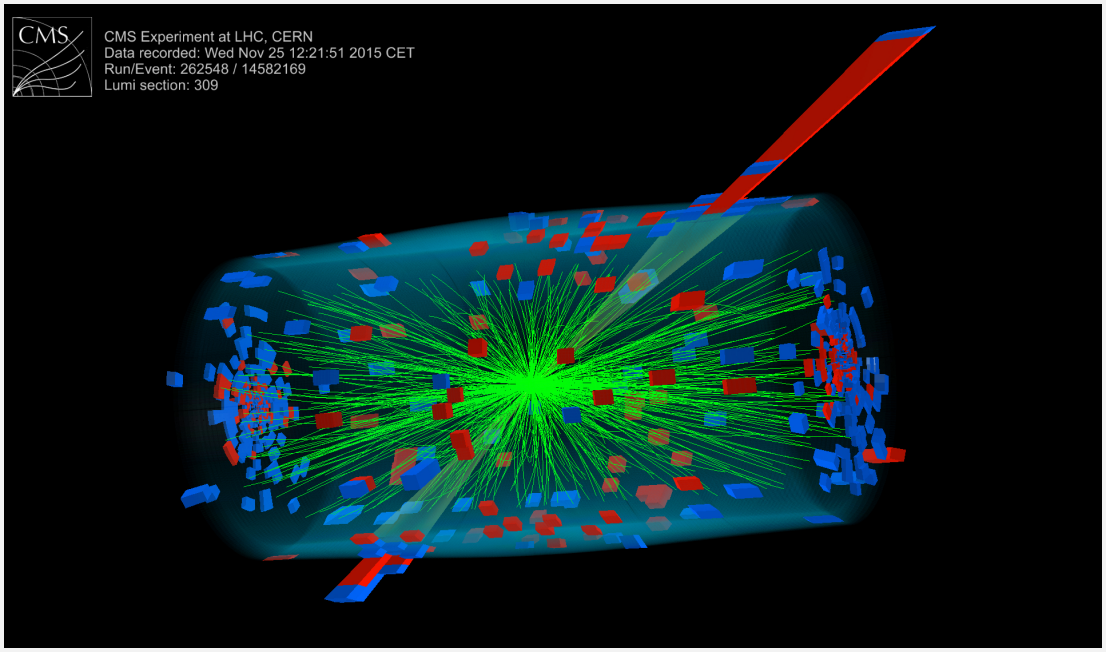

Figure 1.1: One of the first heavy-ion beam collisions recorded at the Compact Muon Solenoid (CMS) detector at the Large Hadron Collider, on the 25th November 2015. *Maximilien Brice*, CERN.

Theory

2.1 - Feynman Diagrams and Particle Interactions

2.1.1. Relativistic Kinematics

We consider the annihilation of a quark-antiquark pair to form a Z-boson. Each of these particles has associated with them some four-momentum p_i (distinguishing between the four-momentum p_i with no decoration, as opposed to physical three-momentum denoted $\vec{p}_i$), of the form

$$p_i = (E_i, (\vec{p}_i)_x, (\vec{p}_i)_y, (\vec{p}_i)_z) \tag{2.1}$$

which lives in Minkowski space, where the inner product between four-vectors is defined to be

$$a \cdot b = a^\mu g_{\mu\nu} b^\nu = E_a E_b - \vec{p}_a \cdot \vec{p}_b \tag{2.2}$$

where we use the *mostly negative* convention for the Minkowski metric $g_{\mu\nu} = \text{diag}(1, -1, -1, -1)$. Due to extreme energy scales achieved in particle physics, special relativistic effects are important. We therefore use the relativistic energy-momentum equation in natural units

$$p^2 \equiv p \cdot p = E^2 - |\vec{p}|^2 = m^2, \tag{2.3}$$

where m is referred to as the *invariant mass* of the particle. Calculations in particle physics are often done in the center-of-mass frame, which is the reference frame such that all three-momenta of the particles sum to zero,

$$\sum_i \vec{p}_i = 0. \tag{2.4}$$

The convenience of this frame arises when considering the inner product of the sum of these center-of-mass four momenta:

$$\left(\sum_i p_i\right)^2 \equiv \left(\sum_i p_i\right) \cdot \left(\sum_i p_i\right) = \left(\sum_i E_i\right)^2 - \left(\sum_i \vec{p}_i\right)^2 = \left(\sum_i E_i\right)^2, \tag{2.5}$$

and we therefore see that the invariant mass of this center-of-mass system, denoted W, corresponds to the total energy in the system

$$W = E_{\text{CM}} = E_1 + E_2 + ... + E_N. \tag{2.6}$$

Importantly, we used the relativistic energy-momentum relation to define W, and thus will correspond to the invariant mass of the whole system in all frames of reference. The idea of defining physical quantities in a Lorentz invariant manner, meaning they hold the same value in all frames of reference, is used widely throughout particle physics as this provides the utility of choosing a particularly simple frame of reference in which to evaluate a constant, in the knowledge that this result will then hold in all other frames of reference. Which physical quantities are relevant however depends on the configuration of the system.

2.1.2. Feynman Diagrams

Physical particle interactions are described through Feynman diagrams. In these diagrams, incoming particles, called *initial state particles* drawn on the left of the diagram, can interact with each other through internal lines and vertices, called *virtual propagators*, which then flow with time to the right of

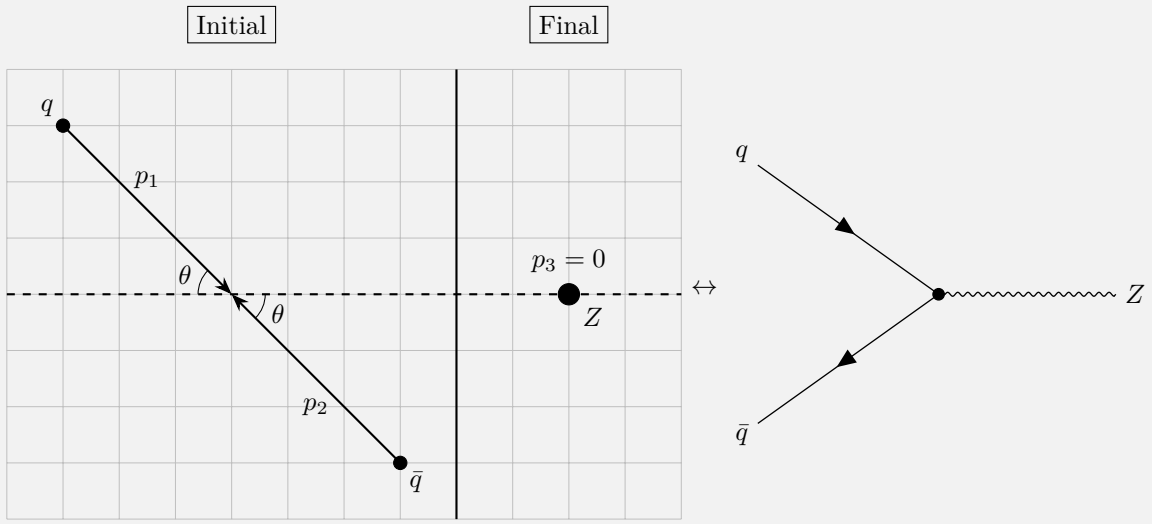

Figure 2.1: *Left:* General configuration of a quark anti-quark pair in the initial state annihilating to form a Z-boson in the final state, within the center-of-mass frame of the Z-boson. *Right:* Corresponding Feynman diagram for the $q\bar{q} \to Z$ process. The Feynman diagram does not depend on a particular frame.

the diagram where outgoing particles, called *final state particles*, can be found. The internal propagators are referred to as *virtual* as they are never physically observed. They are only the means by which initial state particles physically translate into final state particles.

Considering the process of quark annihilation into a Z-boson, denoted $q\bar{q} \to Z$, the left side of Figure 2.1 depicts a general configuration of the initial state quarks and final state Z-boson, in the center-of-mass frame. The joint constraints that we are in the center-of-mass frame, combined with energy-momentum conservation, imply that this entire system is parametrised by two degrees of freedom, namely θ and an azimuthal ϕ. The right side depicts the corresponding Feynman diagram of the $q\bar{q} \to Z$ process. We observe that there are no internal propagators in this Feynman diagram, as the direct annihilation process is allowed.

Figure 2.2 depicts two different structures that occur within Feynman diagrams. On the left-hand side is an *s-channel* process, where particles a and b annihilate to form a virtual particle, which then at a later point decays into particles c and d. On the right-hand side is a *t-channel* process, where particles a and c scatter off each-other after interacting through the virtual particle. Taking an example from QED, electron scattering $e^-e^- \to e^-e^-$ involves a T-channel process wherein the electrons repel each-other by interacting through a virtual photon.

Energy-momentum conservation implies that total four-momentum is conserved from the initial state into the final state. For both processes in Figure 2.2, this means that

$$p_a + p_b = p_c + p_d. \tag{2.7}$$

Specifically, denoting the four-momentum of the virtual particle as P_s and P_t for the s and t channel diagrams respectively, we can determine the four-momentum of the virtual propagators as

$$\text{s channel:} \quad P_s = p_a + p_b = p_c + p_d, \tag{2.8}$$

$$\text{t channel:} \quad P_t = p_a - p_c = p_b - p_d. \tag{2.9}$$

In the case of s channel processes, we see that $P_s = p_a + p_b$ corresponds to the total four-momenta of the initial state and therefore we have $W^2 = E_{\text{CM}}^2 = P_s^2$.

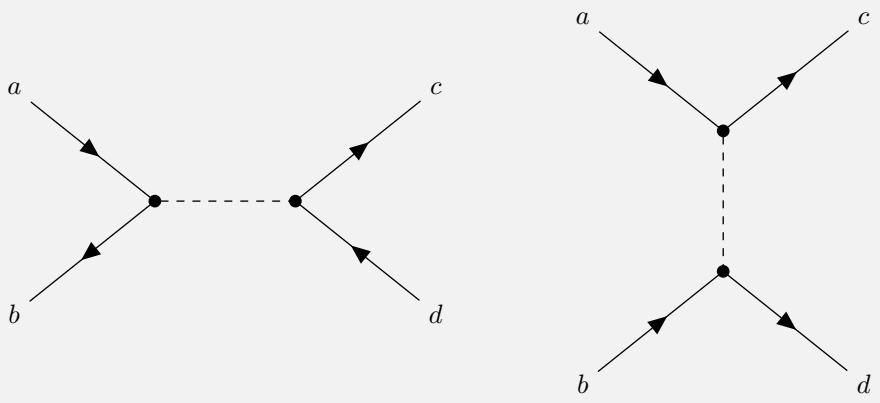

Figure 2.2: Two types of Feynman diagrams: S-channel processes (left) and T-channel processes (right). Time flows from left to right, with external legs connected through virtual propagators. In both cases the total center-of-mass energy squared is given by $s = (p_a + p_b)^2$.

2.1.3. Mandelstam Variables

One family of kinematic variables used widely throughout this project are the *Mandelstam variables*. Again considering the particles of Figure 2.2, the Mandelstam variables are defined as

$$s = (p_a + p_b)^2, \tag{2.10}$$

$$t = (p_a - p_c)^2, \tag{2.11}$$

$$u = (p_a - p_d)^2. \tag{2.12}$$

For more complicated processes, the Mandelstam variables are explicitly denoted with respect to the particles they describe, for example $s_{ab} = (p_a + p_b)^2$ and $t_{ij} = (p_i - p_j)^2$. We can also introduce a Mandelstam s variable for three particles, such that

$$s_{ijk} = (p_i + p_j + p_k)^2. \tag{2.13}$$

As these variables are described as the square of some four-momenta, they can be written in the form

$$s_{ab} = (p_a + p_b) \cdot (p_a + p_b) = ((p_a)^\mu + (p_b)^\mu)\left((p_a)_\mu + (p_b)_\mu\right). \tag{2.14}$$

The indices of these terms are therefore fully contracted, meaning that these Mandelstam variables are Lorentz invariant quantities. This can also be seen by considering the processes of Figure 2.1; considering the *S-channel* process, we have that $W^2 = (p_a + p_b)^2 = s$ and so the Mandelstam s variable corresponds to the square of the center-of-mass energy in the system.

2.1.4. Matrix Elements

Each Feynman diagram corresponds to a mathematical expression that can be derived using the laws of QED and QCD, however in practice these laws have been abstracted to the level of *Feynman rules* which prescribe factors for each element of the Feynman diagram that can be combined to give the full expression. To create a complete picture for some given interaction, all the possible Feynman diagrams for that process must be considered. The mathematical expressions from all possible Feynman diagrams can then be combined to create the corresponding squared matrix element, which can be interpreted as a probability density for the process, given some physical particle configuration.

Generally speaking, we can consider a system of particles $|\Psi_i\rangle$ that undergo some interaction $\hat{U}$, after which we want to know the probability that these particles finish in some final state $|\Psi_f\rangle$. The matrix element for this process is denoted

$$\mathcal{M}_{fi} = \langle \Psi_f | \hat{U} | \Psi_i \rangle, \tag{2.15}$$

such that the probability density of this process is given by

$$P(\text{Initial} \to \text{Final}) \propto |\mathcal{M}_{fi}|^2 = \left| \langle \Psi_f | \hat{U} | \Psi_i \rangle \right|^2. \tag{2.16}$$

In the context of particle physics, $\langle \Psi_f | \hat{U} | \Psi_i \rangle$ are expressed in terms of Feynman diagrams such that we can model particle interactions in the same manner, as demonstrated in Equation 2.17 for quark-antiquark annihilation into a Z-boson. Note that Feynman diagrams are left in pictorial form when they appear in equations, as their corresponding mathematical expressions can be quite complex.

$$P\left(q\bar{q} \to Z\right) \propto \left|\mathcal{M}_{fi}\left(p_q, p_{\bar{q}}, p_Z\right)\right|^2 = \left| \right|^2 . \tag{2.17}$$

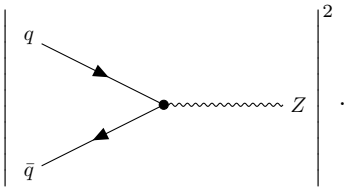

In general however, there are many Feynman diagrams for a particular process and therefore as the squared matrix element is a probabilistic quantity, it must take into consideration all possible diagrams. Considering the process of quark-antiquark annihilation into a Z-boson and a gluon, denoted $q\bar{q} \to Zg$, there are two possible Feynman diagrams for this process wherein the gluon can be emitted from either quark or antiquark, as shown below in Equation 2.18,

$$P\left(q\bar{q} \to Zg\right) \propto \left|\mathcal{M}_{fi}\left(p_q, p_{\bar{q}}, p_Z, p_g\right)\right|^2 = \left| \right|^2 . \tag{2.18}$$

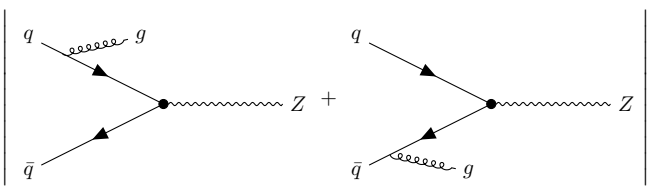

When multiple Feynman diagrams must be taken into account for a given process, squaring the matrix elements results in a cross-multiplication between different Feynman diagrams in the final result. The mathematical expressions of these diagrams are complex numbers, and so this cross-multiplication results in *interference effects* between different diagrams.

We also observe that for processes involving a high number of particles, there are many more possible Feynman diagrams contribute to the process, and so the complexity of the final expression grows considerably and rapidly.

2.2 - Parton Showers

Due to this relationship between number of particles and increase in mathematical complexity in matrix element calculations, evaluating the matrix element for an entire parton shower containing multitudes of bremsstrahlung is not a viable option. One approach to modelling the cascaded emission observed in parton showers is through an iterative picture.

2.2.1. Antenna Functions

Matrix elements have known, general singularity structures. The nature of these singularities is further explored in Section 3.1, however this known singularity structure can be exploited; near the singularities, it will be those singular terms that start to dominate, such that an object called the *splitting function* can be factorised out of the matrix element. In this project, we explore one type of splitting function referred to as an *antenna function*. Naturally, different interactions involve different singularity structures, and therefore different antenna functions can be derived for different processes. In the context of a parton shower algorithm, we can expand around the singularities created by the emission of a gluon, as happens through physical bremsstrahlung. By factoring out the gluon antenna function, we isolate the effect of gluon emission from the underlying, simpler matrix element, called the *Born-level* matrix element. This process is depicted in Figure 2.3 for the case of gluon emission from a quark-antiquark pair, before they annihilate to form a Z-boson.

We can directly compare this to the matrix element calculation shown in Equation 2.18; already we observe the simplification of only having to multiply a much simpler matrix element by this antenna function, as opposed to what would otherwise be the calculation of two, more complicated Feynman diagrams.

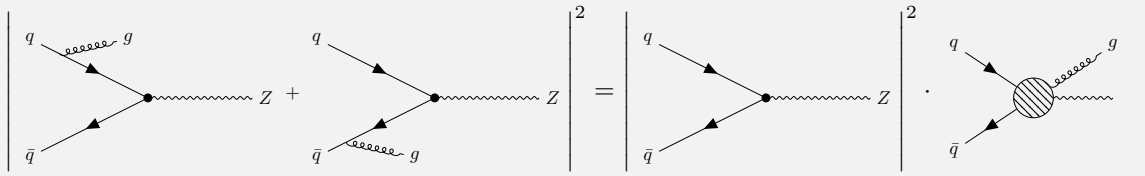

(2.19)

Figure 2.3: Factorisation of the $q\bar{q} \to Zg$ process into the $q\bar{q} \to Z$ matrix element and the antenna function for single-gluon emission, A_3^0.

Having isolated the effect of gluon emission, this antenna function is iteratively applied through parton shower algorithms to model the jets of particles seen in particle detectors. The same factorisation process can be applied in the case of double-gluon emission, to isolate the effect of this double emission from the Born-level matrix element. In this project, explore the structure of both single and double-gluon emission antenna functions in Chapter 3.

2.3 - Crossing Symmetry

The utility of antenna functions lies not only in how they isolate the effect of particle emission, they can also be applied to the family of processes that share a simialar singularity structure, beyond the original process from which it was factorised. Considering the single-gluon emission antenna function, we can apply this to any process from which a gluon is emitted from a quark-antiquark pair in the initial state, for example the $q\bar{q} \to Hg$ process. There is a caveat however, in that to directly apply this antenna function, the quarks from which this gluon emission is achieved must be in the initial state. To extend the applicability of previously derived antenna functions, we can take advantage of an underlying symmetry of matrix elements known as crossing symmetry.

Crossing symmetry refers to an invariance of particle physics wherein the same matrix element of a process with some particle a in the *initial state*, can be used to describe the same process where the corresponding antiparticle $\bar{a}$ appears in the *final state*, with negated four-momenta. The reverse is also true, such that generally speaking, interchanging between particles and antiparticles and negating their momenta allows *crossing* between initial and final states.

Considering the S-channel process of electron scattering $e^-e^- \to e^-e^-$, we can cross one of the initial-state electrons into the final-state by negating its momentum and replacing it with a positron, and similarly cross a final-state electron into an initial-state positron, such that we recover the T-channel process of electron-positron annihilation $e^-e^+ \to e^-e^+$. This is depicted in Figure 2.4. As these processes are connected through crossing symmetry, they can be described by the same underlying function.

As antenna functions are derived from matrix elements, they also obey crossing symmetry. This means that the antenna function for gluon emission from a quark-antiquark pair in the initial state can be crossed into an antenna function describing gluon emission from a quark-antiquark pair in the final state, enabling more flexibility in what processes this antenna function can be applied to.

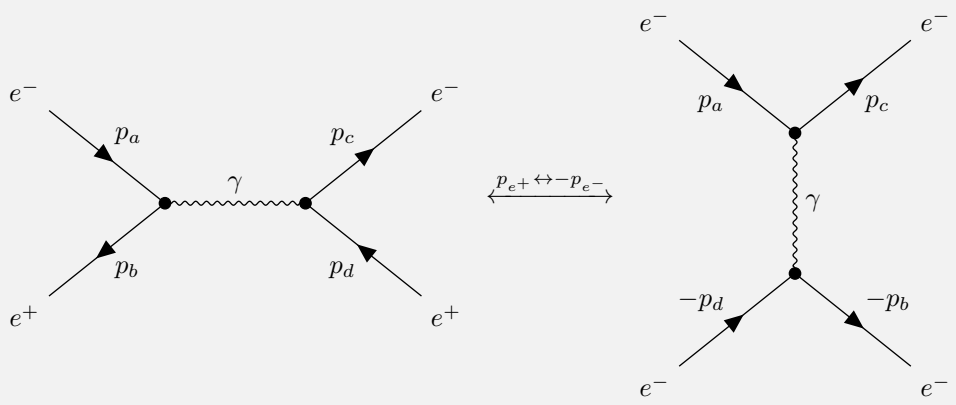

Figure 2.4: The same mathematical functions can be used when modelling electron-positron annihilation $e^-e^+ \to e^-e^+$ and electron scattering $e^-e^- \to e^-e^-$, as these processes are related by crossing symmetry.

Analysis & Results

3.1 - The A_3^0 Antenna Function

We first explore the structure and limits of the single-gluon emission antenna function for a quark-antiquark in the final state, which is denoted A_3^0 in [5]. Labelling the final state quark 1, the anti-quark as 2 and the emitted gluon as 3, A_3^0 is given as [5]

$$A_3^0(p_1, p_2, p_3) = \frac{1}{s_{123}}\left(\frac{s_{13}}{s_{23}} + \frac{s_{23}}{s_{13}} + 2\frac{s_{12}s_{123}}{s_{13}s_{23}}\right). \tag{3.1}$$

We explicitly observe s_{13} and s_{23} in the denominator of A_3^0, and we therefore want to characterise physical configurations where these variables are small enough that the antenna functions becomes singular, as these are the physical configurations which will likely be most abundantly observed. Parton showers are modelled occurring at energies on the order of GeV and TeV, while the quarks we model have mass far below this energy scale. We therefore assume that we are in the *ultra-relativistic limit*, wherein the masses of these particles can be neglected as they are insignificant compared to their respective momenta. Examining the structure of Mandelstam variables in the ultra-relativistic limit, we see that

$$\begin{aligned} s_{ij} &= (p_i + p_j)^2 & t_{ij} &= (p_i - p_j)^2 \\ &= p_i^2 + 2p_i \cdot p_j + p_j^2 & &= p_i^2 - 2p_i \cdot p_j + p_j^2 \\ &= m_i^2 + 2p_i \cdot p_j + m_j^2 & &= m_i^2 - 2p_i \cdot p_j + m_j^2 \\ &= 2p_i \cdot p_j, & &= -2p_i \cdot p_j. \end{aligned}$$

when $m_i = m_j = 0$. For the remaining discussion, we assume the ultra-relativistic limit such that $s_{ij} = 2p_i \cdot p_j$ as above, due to the fact that quarks within the colliding proton beams are usually low mass and carry extremely high momenta. Using this, we have

$$\begin{aligned} s_{123} &= (p_1 + p_2 + p_3)^2 \\ &= p_1^2 + p_2^2 + p_3^2 + 2p_1 \cdot p_2 + 2p_1 \cdot p_3 + 2p_2 \cdot p_3 \\ &= s_{12} + s_{13} + s_{23}. \end{aligned}$$

Using the Minkowski product, we know

$$\begin{aligned} p_i \cdot p_j &= E_i E_j - \vec{p_i} \cdot \vec{p_j} \\ &= E_i E_j - |\vec{p_i}||\vec{p_j}| \cos\theta_{ij}, \end{aligned}$$

where θ_{ij} is the angle between particles i and j. Here, we can use relativistic energy-momentum conservation for massless particles, giving $E_i = |\vec{p_i}|$ such that

$$p_i \cdot p_j = E_i E_j (1 - \cos\theta_{ij}). \tag{3.2}$$

We therefore see that A_3^0 will become singular in the limit of *soft radiation*, where $E_3 \to 0$, or *collinear radiation*, where either $\theta_{13} \to 0$ or $\theta_{23} \to 0$.

3.1.1. Soft Radiation

Soft radiation of gluon 3 is parametrised first through the substitution $p_3 \to \lambda p_3$ and then taking a series expansion of $A_3^0(\lambda)$ in the limit $\lambda \to 0$. We first examine the impact of these λ substitutions on the Mandelstam variables;

$$s_{12} = 2p_1 \cdot p_2 \to 2p_1 \cdot p_2 = s_{12}, \tag{3.3}$$
$$s_{13} = 2p_1 \cdot p_3 \to 2p_1 \cdot \lambda p_3 = \lambda s_{13}, \tag{3.4}$$
$$s_{23} = 2p_2 \cdot p_3 \to 2p_2 \cdot \lambda p_3 = \lambda s_{23}. \tag{3.5}$$

We therefore make the substitutions $s_{13} \to \lambda s_{13}$ and $s_{23} \to \lambda s_{23}$, then taking the first three terms of the Laurent expansion to get

$$\lim_{\lambda \to 0} A_3^0(\lambda) = \frac{2s_{12}}{\lambda^2 s_{13} s_{23}} + \frac{s_{13}^2 + s_{23}^2}{s_{12} s_{13} s_{23}} - \frac{\lambda(s_{13} + s_{23})\left(s_{13}^2 + s_{23}^2\right)}{s_{12}^2 s_{13} s_{23}} + \mathcal{O}\left(\lambda^3\right). \tag{3.6}$$

We can therefore see that in the limit of soft radiation,

$$A_3^0 \to \frac{2s_{12}}{s_{13} s_{23}}, \tag{3.7}$$

and this is referred to as the Eikonal or Dipole factor [2].

3.1.2. Collinear Radiation

Collinear radiation of particle 3 means that either $\theta_{13} \to 0$ or $\theta_{23} \to 0$. We examine the limit of particles 3 and 1 becoming collinear, with the results being easily interchangeable between particles 1 and 2.

The limit of $\theta_{13} \to 0$ impacts only the s_{13} invariant, wherein

$$\lim_{\theta_{13} \to 0} s_{13} = \lim_{\theta_{13} \to 0} 2E_1 E_3 (1 - \cos\theta_{13}) = 0. \tag{3.8}$$

The limit of collinear radiation is therefore sufficiently parametrised by the substitution $s_{13} \to \lambda s_{13}$, followed again by a series expansion about $\lambda \to 0$, given below

$$\lim_{\theta_{13} \to 0} A_3^0(\lambda) = \frac{2s_{12}^2 + 2s_{12}s_{23} + s_{23}^2}{\lambda s_{13} s_{23}(s_{12} + s_{23})} + \frac{\lambda s_{13}}{s_{23}(s_{12} + s_{23})}. \tag{3.9}$$

In this limit where $\theta_{13} \approx 0$, the four-momenta p_1 and p_3 become linearly dependent. Considering a particle I with momentum $p_I = p_1 + p_3$ wherein I radiates gluon 3 and thereafter is denoted particle 1, the linear dependence of these final momenta can be established by first defining a momentum fraction $z \in [0, 1]$, such that the radiated gluon has momentum zp_I, leaving the remaining $(1 - z)p_I$ for particle 1. Linear dependence of these momenta are thus achieved, as they are scalar multiples of the same p_I. Inserting these linearly dependent momenta into the Mandelstam variables, we see that

$$s_{12} = 2p_1 \cdot p_2 \to 2(1 - z)p_I \cdot p_2 = (1 - z)s_{I2}, \tag{3.10}$$
$$s_{23} = 2p_2 \cdot p_3 \to 2p_2 \cdot zp_I = zs_{I2}. \tag{3.11}$$

Making these substitutions into the first term of the Laurent series above, we have the form of A_3^0 in the limit of collinear radiation

$$\lim_{\theta_{13} \to 0} A_3^0 = \frac{1}{s_{13} z}\left(2 - 2z + z^2\right), \tag{3.12}$$

which agrees with the form stated in [5].

3.2 - The A_4^0 Antenna Function

We now explore the $q\bar{q} \to Zgg$ process, with gluon emission from quarks in the initial state. The corresponding double-gluon emission antenna function is denoted A_4^0 in [5] and is depicted in Figure 3.1.

The function A_4^0 for double-gluon emission from quarks in the final state is provided in [5], therefore the desired initial state function can be obtained through crossing symmetry. The final state A_4^0 quark

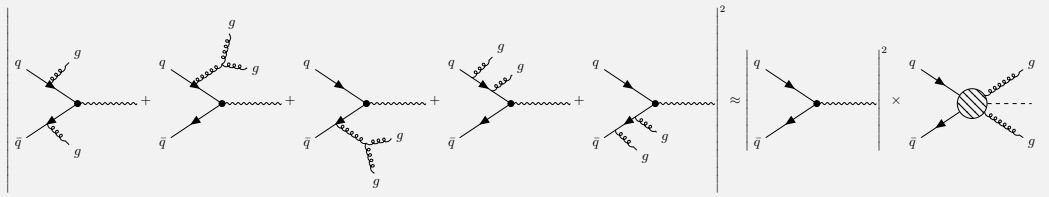

Figure 3.1: Factorisation of the $q\bar{q} \to Zgg$ matrix element using the double-gluon emission antenna function, A_4^0.

and antiquark are denoted particles 1 and 2 respectively, with the gluons denoted 3 and 4. To differentiate between particles in the initial and final states, a different notation is used in the crossed A_4^0, with the initial state quarks denoted a and b respectively, with the gluons denoted j and k.

In the notation of [5], an overall factor of s_{1234} appears in A_4^0 which denotes a four-particle Mandelstam variable. To simplify later substitutions, we expand this as

$$\begin{aligned} s_{1234} &= (p_1 + p_2 + p_3 + p_4)^2 \\ &= s_{12} + s_{13} + s_{14} + s_{23} + s_{24} + s_{34}. \end{aligned}$$

We now compare the conservation equations for these initial and final-state processes,

$$\text{Final-state process } Z \to qgg\bar{q} \qquad p_Z = p_1 + p_2 + p_3 + p_4, \tag{3.13}$$

$$\text{Final-state process } q\bar{q} \to Zgg \quad p_a + p_b = p_Z + p_j + p_k. \tag{3.14}$$

The required crossing substitutions are therefore

$$\begin{aligned} p_1 \to -p_b, \quad p_3 \to p_j, \\ p_2 \to -p_a, \quad p_4 \to p_k, \end{aligned}$$

where the last two substitutions are purely notational. Note that p_Z is not explicitly changed, as it is fully prescribed by fixing all other momenta. These substitutions are visualised in Figure 3.2 We can then use these momentum-level substitutions and determine substitutions at the level of Mandelstam variables;

$$s_{12} = (p_1 + p_2)^2 \to (-p_a - p_b)^2 = s_{ab}, \tag{3.15}$$

$$s_{13} = (p_1 + p_3)^2 \to (-p_a + p_j)^2 = -s_{aj}, \tag{3.16}$$

$$s_{14} = (p_1 + p_4)^2 \to (-p_a + p_k)^2 = -s_{ak}, \tag{3.17}$$

$$s_{23} = (p_2 + p_3)^2 \to (-p_b + p_j)^2 = -s_{bj}, \tag{3.18}$$

$$s_{24} = (p_2 + p_4)^2 \to (-p_b + p_k)^2 = -s_{bk}, \tag{3.19}$$

$$s_{34} = (p_3 + p_4)^2 \to (p_j + p_k)^2 = s_{jk}, \tag{3.20}$$

$$s_{134} = (p_1 + p_3 + p_4)^2 \to (-p_a + p_j + p_k)^2 = -s_{aj} - s_{ak} + s_{jk}, \tag{3.21}$$

$$s_{234} = (p_2 + p_3 + p_4)^2 \to (-p_b + p_j + p_k)^2 = -s_{bj} - s_{bk} + s_{jk}. \tag{3.22}$$

The resulting initial-state A_4^0 antenna function is reported in Appendix 5.

3.2.1. The Double-Soft Limit

Structures arising within the antenna function for single gluon emission, related to important physical configurations achieved by that gluon, also appear in a more general manner for double-gluon emission. Here we have the possibility for not only soft emission of one gluon, but simultaneous soft emission of both gluons, referred to as the *double-soft limit*.

In a similar manner to single-soft emission, the soft emission of both gluons is parametrised by substituting

$$p_j \to \lambda p_j, \quad p_k \to \lambda p_k, \tag{3.23}$$

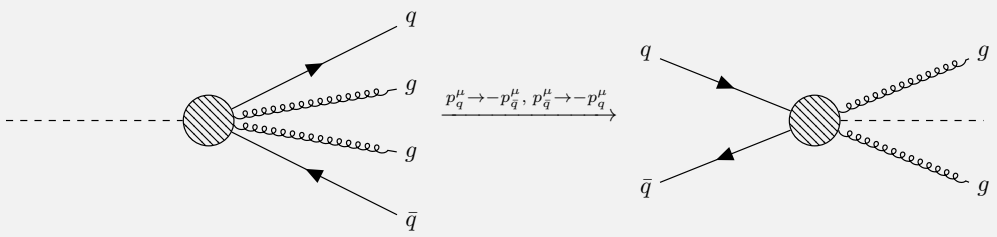

Figure 3.2: *Left:* Feynman diagram where the quark, antiquark and gluons are all in the final state. *Right:* Feynman diagram where the quark and antiquark are in the initial state, with both gluons in the final state. These antenna functions are related through crossing symmetry.

and then expanding around $\lambda = 0$. Determining the Mandelstam variable level effect of these substitutions, we see

$$s_{ab} = (p_a + p_b)^2 \to (p_a + p_b)^2 = s_{ab}, \tag{3.24}$$
$$s_{aj} = (p_a + p_j)^2 \to (p_a + \lambda p_j)^2 = \lambda s_{aj}, \tag{3.25}$$
$$s_{ak} = (p_a + p_k)^2 \to (p_a + \lambda p_k)^2 = \lambda s_{ak}, \tag{3.26}$$
$$s_{bj} = (p_b + p_j)^2 \to (p_b + \lambda p_j)^2 = \lambda s_{bj}, \tag{3.27}$$
$$s_{aj} = (p_b + p_k)^2 \to (p_b + \lambda p_k)^2 = \lambda s_{bk}, \tag{3.28}$$
$$s_{jk} = (p_j + p_k)^2 \to (\lambda p_j + \lambda p_k)^2 = \lambda^2 s_{jk}. \tag{3.29}$$

In the case of single-soft emission, the Mandelstam level variables were at most $\mathcal{O}(\lambda)$, whereas here we see that the substitution $s_{jk} \to \lambda^2 s_{jk}$ is $\mathcal{O}(\lambda^2)$. Therefore, while the Laurent expansion in $\lambda = 0$ for single-soft emission had a singularity of order $\mathcal{O}\left(\frac{1}{\lambda^2}\right)$, we expect the Laurent expansion for double-soft emission to be $\mathcal{O}\left(\frac{1}{\lambda^4}\right)$. This is confirmed in the series expansion where we indeed see a singularity of order $\mathcal{O}\left(\frac{1}{\lambda^4}\right)$. This will therefore be the term that dominates in double-soft configurations, such that the form of A_4^0 in the double soft limit becomes

$$\begin{aligned}
A_4^0 \to\ & \frac{2s_{ab}^2 s_{ak} s_{bj}}{s_{aj} s_{bk} (s_{aj} + s_{ak})^2 (s_{bj} + s_{bk})^2} + \frac{2s_{ab}^2 s_{bj}}{s_{bk} (s_{aj} + s_{ak})^2 (s_{bj} + s_{bk})^2} + \frac{2s_{ab}^2 s_{ak}}{s_{aj} (s_{aj} + s_{ak})^2 (s_{bj} + s_{bk})^2} \\
& + \frac{2s_{ab}^2}{(s_{aj} + s_{ak})^2 (s_{bj} + s_{bk})^2} + \frac{2s_{ab} s_{ak}^2 s_{bj}^2}{s_{aj} s_{bk} s_{jk} (s_{aj} + s_{ak})^2 (s_{bj} + s_{bk})^2} \\
& + \frac{6s_{ab} s_{ak}^2 s_{bj}}{s_{aj} s_{jk} (s_{aj} + s_{ak})^2 (s_{bj} + s_{bk})^2} + \frac{4s_{ab} s_{ak}^2 s_{bk}}{s_{aj} s_{jk} (s_{aj} + s_{ak})^2 (s_{bj} + s_{bk})^2} \\
& + \frac{4s_{ab} s_{aj} s_{bj}^2}{s_{bk} s_{jk} (s_{aj} + s_{ak})^2 (s_{bj} + s_{bk})^2} + \frac{6s_{ab} s_{ak} s_{bj}^2}{s_{bk} s_{jk} (s_{aj} + s_{ak})^2 (s_{bj} + s_{bk})^2} + \frac{2s_{ab} s_{aj} s_{bj}}{s_{jk} (s_{aj} + s_{ak})^2 (s_{bj} + s_{bk})^2} \\
& + \frac{8s_{ab} s_{ak} s_{bj}}{s_{jk} (s_{aj} + s_{ak})^2 (s_{bj} + s_{bk})^2} - \frac{2s_{ab} s_{aj} s_{bk}}{s_{jk} (s_{aj} + s_{ak})^2 (s_{bj} + s_{bk})^2} + \frac{2s_{ab} s_{ak} s_{bk}}{s_{jk} (s_{aj} + s_{ak})^2 (s_{bj} + s_{bk})^2} \\
& + \frac{2s_{aj}^2 s_{bk}^2}{s_{jk}^2 (s_{aj} + s_{ak})^2 (s_{bj} + s_{bk})^2} + \frac{2s_{ak}^2 s_{bj}^2}{s_{jk}^2 (s_{aj} + s_{ak})^2 (s_{bj} + s_{bk})^2} - \frac{4s_{aj} s_{ak} s_{bj} s_{bk}}{s_{jk}^2 (s_{aj} + s_{ak})^2 (s_{bj} + s_{bk})^2}.
\end{aligned} \tag{3.30}$$

3.2.2. The Triple-Collinear Limit

Similarly to the case of collinear emission for a single gluon, within the double-gluon antenna function we can explore the limit of both gluons becoming collinear with their parent, referred to as the *triple collinear limit*.

Thus far, we have labelled the quarks in the initial state a and b respectively, with the gluons in the final state as j and k respectively. As the gluon emission happens from quarks in the initial state, we distinguish between the quark before any emission (the aforementioned a) and the quark after double-gluon emission, denoted by a capital A. The same distinction is made between pre-emission b and

post-emission B. In terms of four-momentum conservation, this can be stated as

$$p_a + p_b = p_A + p_B + p_j + p_k, \tag{3.31}$$

at which point the post-emission quarks annihilate to form the Z-boson

$$p_A + p_B = p_Z. \tag{3.32}$$

In the triple-collinear limit, both gluons are emitted from the same quark and in this way their momenta become collinear, giving rise to singularities in the antenna function as described in the structure of Equation 3.2; strictly speaking, collinear emission of gluon j from quark a alongside collinear emission of gluon k from quark b would lead to an overall anti-collinear configuration, however in this case we have $\theta_{jk} = \pi$, which does not give rise to singularities in the antenna function and therefore is not considered within the triple-collinear limit.

With this in mind, we explore the collinear-emission structure of

$$p_a = p_A + p_j + p_k, \tag{3.33}$$

with the same derivation being directly applicable to collinear emission from antiquark b. With the same justification as in the simpler case of double-collinear emission, the angles θ_{Aj}, θ_{Ak} and θ_{jk} are parametrised going to zero through the Mandelstam variable level substitutions

$$s_{Aj} \to \lambda s_{Aj}, \tag{3.34}$$
$$s_{Ak} \to \lambda s_{Ak}, \tag{3.35}$$
$$s_{jk} \to \lambda s_{jk}, \tag{3.36}$$

enabling then a series expansion around $\lambda \to 0$. However the invariants of A_4^0 are in terms of four-momentum p_a, not p_A as in the above substitutions. We therefore use Equation 3.33 to express the variables in terms of p_A, before using the λ substitutions above. First examining s_{ab}, we see that

$$\begin{aligned} s_{ab} = (p_a + p_b)^2 &= ((p_A + p_j + p_k) + p_b)^2 \\ &= (p_A + p_j + p_k)^2 + p_b^2 + 2p_b \cdot (p_A + p_j + p_k) \\ &\to 2p_b \cdot (p_A + p_j + p_k), \end{aligned}$$

using the fact that b is a massless particle, and

$$s_{Ajk} = (p_A + p_j + p_k)^2 = s_{Aj} + s_{Ak} + s_{jk} \to \lambda (s_{Aj} + s_{Ak} + s_{jk}) \tag{3.37}$$

which therefore goes to zero. To continue, we introduce momentum fractions in an analogous manner to the double-collinear case, such that for collinear particles A, j and k we have

$$p_A \to z_A (p_A + p_j + p_k) = z_A p_a, \tag{3.38}$$
$$p_j \to z_j (p_A + p_j + p_k) = z_j p_a, \tag{3.39}$$
$$p_k \to z_k (p_A + p_j + p_k) = z_k p_a, \tag{3.40}$$

wherein $z_A + z_j + z_k = 1$. In this way, conservation of four-momentum is respected and these particles are now collinear. With these momentum fractions, we see that

$$\begin{aligned} 2p_b \cdot (p_A + p_j + p_k) &\to 2p_b \cdot (z_A p_a + z_j p_a + z_k p_a) \\ &= 2 (z_A + z_j + z_k) p_b \cdot p_a \\ &= s_{ab}, \end{aligned}$$

and we therefore explicitly see that s_{ab} is unchanged in the triple-collinear limit. This is to be expected, as s_{ab} corresponds to the center-of-mass energy squared. Next exploring s_{aj}, we see that

$$\begin{aligned} s_{aj} = (p_a + p_j)^2 &= ((p_A + p_j + p_k) + p_j)^2 \\ &= p_A^2 + 4p_j^2 + p_k^2 + 2s_{Aj} + 2s_{jk} + s_{Ak} \\ &\to 2\lambda s_{Aj} + 2\lambda s_{jk} + \lambda s_{Ak} \\ &= \lambda s_{aj}. \end{aligned}$$

In the exact same manner,

$$s_{ak} = (p_a + p_k)^2 = ((p_A + p_j + p_k) + p_k)^2 \to \lambda s_{ak}. \tag{3.41}$$

The remaining invariants s_{bj} and s_{bk} are unaffected by the λ substitutions, and so all that remains is to substitute the momentum fractions.

$$s_{bj} = (p_b + p_j)^2 \to (p_b + z_j p_a)^2 = z_j s_{ab}, \tag{3.42}$$

$$s_{bk} = (p_b + p_k)^2 \to (p_b + z_k p_a)^2 = z_k s_{ab}. \tag{3.43}$$

We can now determine the triple-collinear limit of A_4^0 by inserting these derived substitutions, and then applying a series expansion about $\lambda = 0$. This limit is given below in equation 3.44.

$$\begin{aligned}
A_0^4 \to\ & \frac{2s_{aj}^2}{s_{jk}^2(s_{aj}+s_{ak}-s_{jk})^2} - \frac{2s_{ak}^2}{s_{aj}s_{jk}(s_{aj}+s_{ak}-s_{jk})^2} - \frac{4s_{aj}z_j}{s_{jk}^2(z_j+z_k)(s_{aj}+s_{ak}-s_{jk})} \\
& - \frac{s_{ak}z_j^3}{s_{aj}s_{jk}(z_j-1)(z_j+z_k-1)(s_{aj}+s_{ak}-s_{jk})} + \frac{z_j^3}{s_{jk}(z_j-1)(z_j+z_k-1)(s_{aj}+s_{ak}-s_{jk})} \\
& + \frac{2z_j^2}{s_{aj}(z_j-1)z_k(s_{aj}+s_{ak}-s_{jk})} - \frac{s_{ak}z_j^2}{s_{aj}s_{jk}(z_j-1)z_k(s_{aj}+s_{ak}-s_{jk})} \\
& - \frac{2z_j^2}{s_{jk}(z_j-1)z_k(s_{aj}+s_{ak}-s_{jk})} + \frac{3s_{ak}z_j^2}{s_{aj}s_{jk}(z_j-1)(z_j+z_k-1)(s_{aj}+s_{ak}-s_{jk})} \\
& + \frac{s_{ak}z_j^2}{s_{aj}s_{jk}(z_j+z_k)(s_{aj}+s_{ak}-s_{jk})} - \frac{z_j^2}{s_{jk}(z_j+z_k)(s_{aj}+s_{ak}-s_{jk})} \\
& - \frac{5z_j}{s_{aj}(z_j-1)z_k(s_{aj}+s_{ak}-s_{jk})} + \frac{2s_{ak}z_j}{s_{aj}s_{jk}(z_j-1)z_k(s_{aj}+s_{ak}-s_{jk})} \\
& + \frac{4z_j}{s_{jk}(z_j-1)z_k(s_{aj}+s_{ak}-s_{jk})} - \frac{3s_{ak}z_j}{s_{aj}s_{jk}(z_j-1)(z_j+z_k-1)(s_{aj}+s_{ak}-s_{jk})} \\
& - \frac{z_j}{s_{aj}(z_j+z_k)(s_{aj}+s_{ak}-s_{jk})} - \frac{2s_{ak}z_j}{s_{aj}s_{jk}(z_j+z_k)(s_{aj}+s_{ak}-s_{jk})} + \frac{2z_j}{s_{jk}(z_j+z_k)(s_{aj}+s_{ak}-s_{jk})} \\
& + \frac{6}{s_{aj}(z_j-1)z_k(s_{aj}+s_{ak}-s_{jk})} - \frac{2s_{ak}}{s_{aj}s_{jk}(z_j-1)z_k(s_{aj}+s_{ak}-s_{jk})} \\
& - \frac{4}{s_{jk}(z_j-1)z_k(s_{aj}+s_{ak}-s_{jk})} - \frac{1}{s_{aj}(z_j-1)(z_j+z_k-1)(s_{aj}+s_{ak}-s_{jk})} \\
& + \frac{2s_{ak}}{s_{aj}s_{jk}(z_j-1)(z_j+z_k-1)(s_{aj}+s_{ak}-s_{jk})} + \frac{1}{s_{jk}(z_j-1)(z_j+z_k-1)(s_{aj}+s_{ak}-s_{jk})} \\
& + \frac{2}{s_{aj}(z_j+z_k)(s_{aj}+s_{ak}-s_{jk})} + \frac{2s_{ak}}{s_{aj}s_{jk}(z_j+z_k)(s_{aj}+s_{ak}-s_{jk})} \\
& - \frac{6}{s_{jk}(z_j+z_k)(s_{aj}+s_{ak}-s_{jk})} - \frac{2}{s_{aj}(z_j-1)z_jz_k(s_{aj}+s_{ak}-s_{jk})} \\
& - \frac{2}{s_{aj}z_j(z_j+z_k)(s_{aj}+s_{ak}-s_{jk})} - \frac{s_{jk}}{s_{aj}(s_{aj}+s_{ak}-s_{jk})^2} - \frac{3s_{aj}}{s_{jk}(s_{aj}+s_{ak}-s_{jk})^2} \\
& - \frac{s_{ak}}{s_{jk}(s_{aj}+s_{ak}-s_{jk})^2} + \frac{2s_{ak}}{s_{aj}(s_{aj}+s_{ak}-s_{jk})^2} + \frac{2}{(s_{aj}+s_{ak}-s_{jk})^2} + \frac{2z_j^2}{s_{jk}^2(z_j+z_k)^2}.
\end{aligned} \tag{3.44}$$

3.3 - Phase Space Sampling

3.3.1. Sampling A_4^0

We now validate our initial-state A_4^0, alongside its double-soft and triple-collinear limits. Due to the complexity of the closed-form expression for the matrix element $q\bar{q} \to Zgg$, we perform a numerical comparison of the functions in Figure 3.1. Dividing both sides of Figure 3.1 by the Born-level matrix element such as to isolate the matrix elements on the left-hand side, we evaluate both sides of this equation at uniformly sampled points in their domain, produce a histogram of the values generated by both the ratio of matrix elements, and values generated by A_4^0, wherein we will be able to see how well these values agree.

Given some initial configuration, here being the initial four-momenta of the quark and antiquark, the RAMBO [4] algorithm generates uniformly random four-momenta for the resulting final-state Zgg configuration, whilst respecting energy and momentum conservation. Quark-antiquark annihilation is often discussed in the context of two colliding proton beams, wherein it is between the constituent quarks within the protons of these two opposing beams that the hard interaction occurs. To generate some configuration for the initial-state quarks, we therefore define some variable center-of-mass energy E_{CM}, and from this define the four-momenta of two proton beams, denoted p_1 and p_2, with center-of-mass energy E_{CM}

$$p_1 = \left(\frac{E_{\text{CM}}}{2}, 0, 0, \frac{E_{\text{CM}}}{2}\right), \tag{3.45}$$

$$p_2 = \left(\frac{E_{\text{CM}}}{2}, 0, 0, -\frac{E_{\text{CM}}}{2}\right), \tag{3.46}$$

such that

$$W^2 = (p_1 + p_2)^2 = (E_{\text{CM}}, 0, 0, 0)^2 = E_{\text{CM}}^2 \tag{3.47}$$

as desired. To then simulate the constituent quarks colliding at some fraction of this total beam energy, a (pseudo)random number r is generated between 0 and 1, from which we can define an energy fraction

$$x = \left(1 - \frac{m_Z}{E_{\text{CM}}}\right) \cdot r + \left(\frac{m_Z}{E_{\text{CM}}}\right), \tag{3.48}$$

which is then applied to both beam momenta p_1 and p_2 which simulates collision of quarks within carrying some fraction of the total momentum of the beam. To justify our definition of x, we examine the centre-of-mass energy of the quark collision within these two proton beams, given by

$$\hat{W}^2 = (xp_1 + xp_2)^2 = x^2 E_{\text{CM}}^2, \tag{3.49}$$

such that $\hat{W} = \hat{E}_{\text{CM}} = xE_{\text{CM}}$. From its definition, this energy fraction is bounded between

$$\frac{m_Z}{E_{\text{CM}}} \leq x \leq 1. \tag{3.50}$$

In the case of $x = 1$, we have $\hat{E}_{\text{CM}} = E_{\text{CM}}$ such that the quarks are colliding with the full momentum of its proton. Conversely, the lower bound of $x = m_Z/E_{\text{CM}}$ corresponds to $\hat{E}_{\text{CM}} = m_Z$, which is kinematically the lowest possible energy the quark system can take in order to be able to produce the Z-boson. This definition of x therefore ensures that we randomly sample different quark momenta, whilst still having enough energy in the collision to produce the desired $q\bar{q} \to Zgg$ process.

We can therefore define the quark momenta $p_a = xp_1$ and $p_b = xp_2$, from which the RAMBO algorithm can generate p_Z, p_j and p_k. Using these momenta, we can apply MadGraph matrix elements [1] without requiring their closed-form expressions. Both RAMBO and MadGraph are interfaced through their implementation in *Pythia 8.3* [6]. The resulting histogram of values from both sides of this equation, evaluated at 10^7 phase-space points with $E_{\text{CM}} = 10\text{TeV}$ and binned on a logarithmic x-axis in 500 bins between 0 and -12, are plotted in Figure 3.3. We observe that values using the antenna function indeed align with those evaluated from the matrix elements.

We can also explore what effect changing the center-of-mass energy E_{CM} has on the distribution of values produced. Kinematically, the centre-of-mass energy must be at least $m_Z = 91.19\text{GeV}$ in order to be able to produce the Z-boson. We therefore sample with $E_{\text{CM}} = 100\text{GeV}$ such that a Z-boson can be produced alongside the gluons. We also choose to sample with $E_{\text{CM}} = 10\text{TeV}$ to replicate the energy scales currently being achieved at the LHC. An intermediate energy $E_{\text{CM}} = 1\text{TeV}$ is also used as a half-way point between these upper and lower bounds.

Thus far, we have explored A_4^0 as a function only of the particle momenta. However, [5] presents the double-gluon antenna function with dependence also on an ϵ parameter, where ϵ represents how close we are to the singularities around which the antenna function was derived. Setting $\epsilon = 0$ represents a domain in which the antenna function is most valid, with increasing values of ϵ moving further from these singularities. We therefore also produce histograms for ϵ values of 0.3, 0.2 and finally 0 to examine

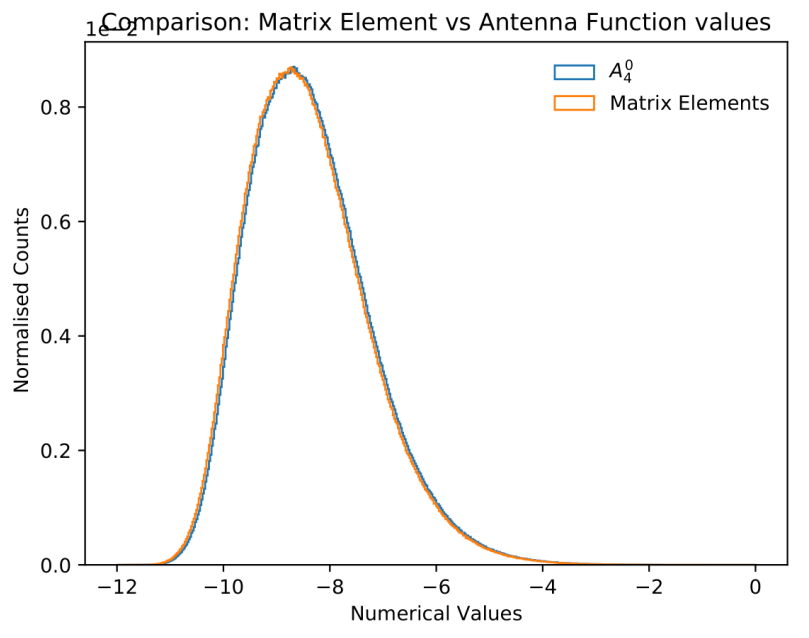

Figure 3.3: Histogram of values generated by the A_4^0 antenna function, alongside values generated from the ratio $|\mathcal{M}_{fi}|^2_{\text{full}}/|\mathcal{M}_{fi}|^2_{\text{Born}}$ at uniformly sampled points in their domain, for a center-of-mass energy $E_{\text{CM}} = 10\text{TeV}$ and plotted on a logarithmic x-axis. Agreement between these histograms demonstrates a correctly factorised A_4^0 antenna function.

changes in the histogram distribution as we approach $\epsilon = 0$.

Denoting the full $q\bar{q} \to Zgg$ matrix element as $|\mathcal{M}_{fi}|^2_{\text{full}}$ and the Born-level matrix element as $|\mathcal{M}_{fi}|^2_{\text{Born}}$ such that the factorisation of Figure 3.1 can be written as

$$|\mathcal{M}_{fi}|^2_{\text{full}} = |\mathcal{M}_{fi}|^2_{\text{Born}} \cdot A_4^0, \tag{3.51}$$

we rearrange this equation

$$\frac{|\mathcal{M}_{fi}|^2_{\text{Born}} \cdot A_4^0}{|\mathcal{M}_{fi}|^2_{\text{full}}} = 1 \tag{3.52}$$

and therefore sample computed values of the fraction on the left-hand side. From this theoretical equation, we expect the histograms to form delta-function distributions about zero (due to being plotted on a logarithmic x-axis). The results of this sampling are shown in Figure 3.4 with values being placed into 100 bins between -0.2 and 0.2. We indeed observe the histogram distributions converging toward a delta-function distribution about $x = 0$ as $\epsilon \to 0$, further validating our initial-state A_4^0 antenna function.

3.3.2. Sampling the *double-soft* and *triple-collinear* limits

We can not directly apply the uniform sampling method of Section 3.3.1, as only a subset of points in the domain of these functions can be considered as corresponding to double-soft or triple-collinear configurations. We therefore establish cuts in the phase space of these functions, to distinguish whether a given point corresponds to either of these limits.

These cuts are based on dimensionless invariants, given as

$$y_{ajk} = \left|\frac{s_{aj} + s_{ak} + s_{jk}}{s_{ab} + s_{jk}}\right|, \quad y_{bjk} = \left|\frac{s_{bj} + s_{bk} + s_{jk}}{s_{ab} + s_{jk}}\right|. \tag{3.53}$$

Considering the configuration where a, j and k are triple-collinear, we showed in Section 3.2.2 that invariants s_{aj}, s_{ak} and s_{jk} will all be small with respect to the center-of-mass energy s_{ab}, and therefore

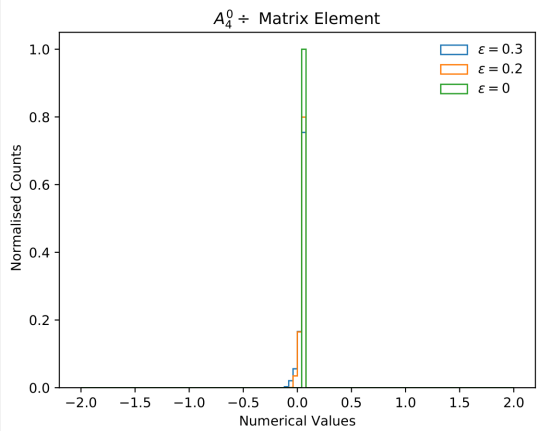

(a) $E_{\text{CM}} = 100\text{GeV}$

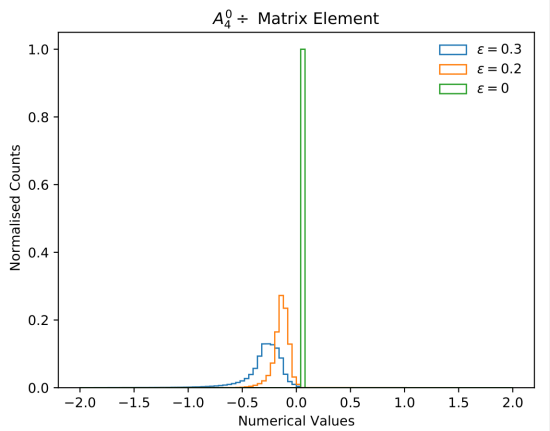

(b) $E_{\text{CM}} = 1\text{TeV}$

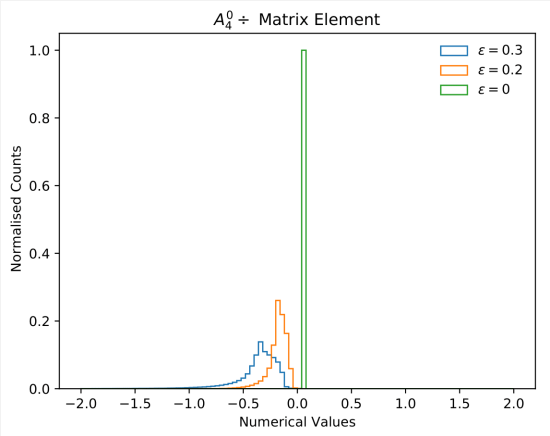

(c) $E_{\text{CM}} = 10\text{TeV}$

Figure 3.4: Histogram of $|\mathcal{M}_{fi}|^2_{\text{Born}} \cdot A_4^0 / |\mathcal{M}_{fi}|^2_{\text{full}}$ evaluated at uniformly random distributed points in their domain, plotted on a logarithmic x-axis with 100 bins between -2 and 2. As $\epsilon \to 0$, distributions converge toward a delta-function at 0 as expected from the factorisation relation. The counts in these plots are normalised such that they sum to unity.

we expect y_{ajk} to be small in the ajk triple-collinear limit. At the same time, invariants s_{bj} and s_{bk}, while dependent on momentum fractions z_j and z_k, are not expected to be small with respect to s_{ab}. We therefore distinguish the ajk triple-collinear limit as points in the domain where $y_{ajk} \leq \delta$ for some appropriately small cutoff δ, whilst $y_{bjk} > \delta$. Similarly, in the bjk triple-collinear limit, we expect $y_{bjk} \leq \delta$ whilst $y_{ajk} > \delta$.

We can also consider the case where both y_{ajk} and y_{bjk} are small with respect to s_{ab}. This implies that the momenta p_j and p_k are small when compared to p_a and p_b, and therefore corresponds to the double-soft configuration. We therefore establish the phase space cut for this limit as both $y_{ajk} < \delta$ and $y_{bjk} < \delta$.

Applying these phase space cuts with $\delta = 0.003$ we generate particle four-momenta as in Section 3.3.1, establish if the configuration is either triple-collinear or double-soft and if so, bin values from the corresponding limit, with respect to Equation 3.52. This sampling method is applied over the same 10^7 phase-space points, with values being placed into 100 bins between -0.25 and 0.25. While we still expect the functions to form delta-distributions about 0, precisely what fractions of the 10^7 phase-space points we expect to represent double-soft or triple-collinear configurations will vary as a function of E_{CM}. Considering $E_{\text{CM}} = 100\text{GeV}$, production of the Z-boson with mass $m_Z = 91.19\text{GeV}$ means there is not much kinematic freedom for the emitted gluon. As a result, we expect that a much larger fraction of the phase-space points will be either double-soft or triple-collinear when sampling with $E_{\text{CM}} = 100\text{GeV}$ as

opposed to $E_{\text{CM}} = 10\text{TeV}$, as there will be much less momentum available for the gluons to take from the interaction.

The resulting histograms for this phase-space sampling of the double-soft and triple-collinear limits of A_4^0 are presented in Figure 3.5, alongside the number of points these functions were sampled at (those satisfying the corresponding δ condition). We again observe convergence of the histogram distributions toward a delta-function centered about 0 for $\epsilon \to 0$. We do however observe a spreading of the triple-collinear limit distribution with increasing energy scale, however they are all dominated by the delta-function shaped peak near zero.

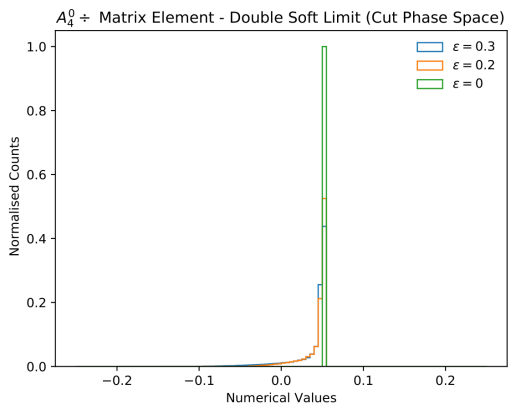

(a) $E_{\mathrm{CM}} = 100\mathrm{GeV}$, $N = 250974$

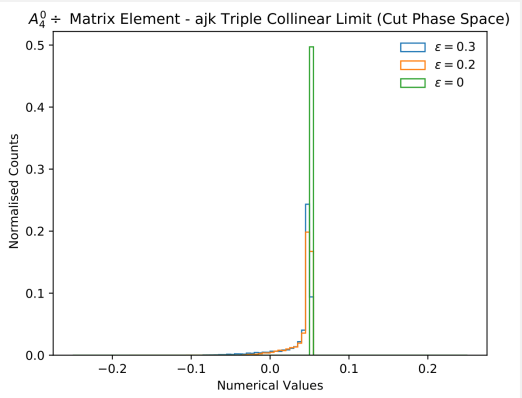

(b) $E_{\mathrm{CM}} = 100\mathrm{GeV}$, $N = 272863$

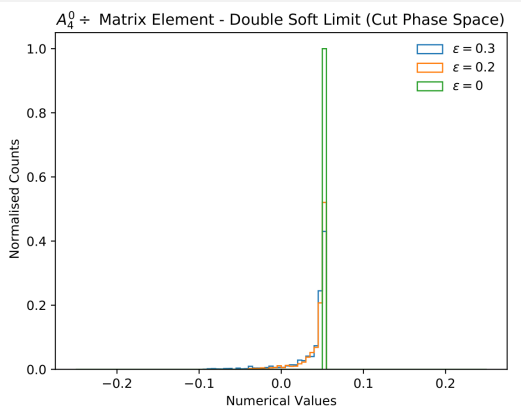

(c) $E_{\mathrm{CM}} = 1\mathrm{TeV}$, $N = 2432$

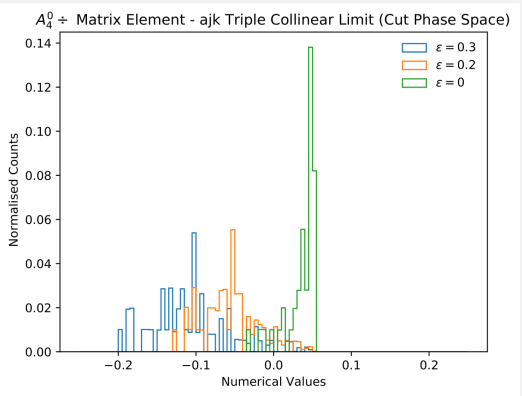

(d) $E_{\mathrm{CM}} = 1\mathrm{TeV}$, $N = 2783$

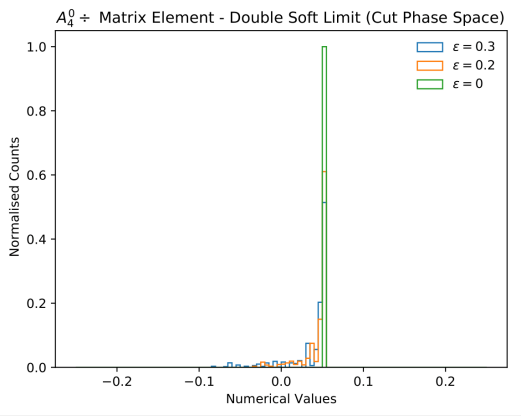

(e) $E_{\mathrm{CM}} = 10\mathrm{TeV}$, $N = 229$

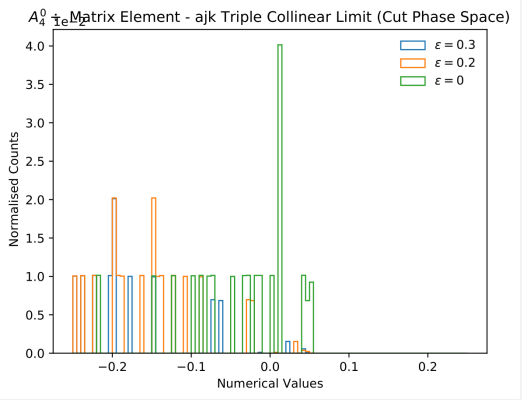

(f) $E_{\mathrm{CM}} = 10\mathrm{TeV}$, $N = 358$

Figure 3.5: Histograms of $|\mathcal{M}_{fi}|^2_{\mathrm{Born}} \cdot A_4^0 / |\mathcal{M}_{fi}|^2_{\mathrm{full}}$, where phase-space cuts have been introduced with $\delta < 0.003$ and the corresponding double-soft or triple-collinear limit of A_4^0 has been substituted, plotted on a logarithmic x-axis with 100 bins between -0.25 and 0.25. We again see that the distributions are dominated by a δ-function near $x = 0$ as $\epsilon \to 0$. The counts in these plots are normalised such that they sum to unity.

Discussion

When sampling the double-soft and triple-collinear functions, it is important that the cutoff invariants y and δ cutoff value are used cohesively, such that as many points can be sampled as possible in order to validate these functions, while still ensuring that these points lie within the appropriate phase-space regions. The form of the dimensionless invariants y_{ajk} and y_{bjk} given in Equation 3.53 are actually the invariants used for quark pairs in the final state. It therefore seems natural that to find the corresponding invariant for quark pairs in the initial state, we should apply the crossing substitutions from Equation 3.22. This would lead to invariants

$$y_{ajk} = \left| \frac{-s_{aj} - s_{ak} + s_{jk}}{s_{ab} + s_{jk}} \right|, \quad y_{bjk} = \left| \frac{-s_{bj} - s_{bk} + s_{jk}}{s_{ab} + s_{jk}} \right|. \tag{4.1}$$

While applying the phase space cut $y_{ijk} < \delta$ here does still capture the required limits wherein s_{ij}, s_{ik} and s_{jk} are all arbitrarily small with respect to s_{ab}, it also captures an extra limit where $s_{jk} \approx s_{ij} + s_{ik}$. This can be re-arranged to give

$$\sin^2\left(\frac{\theta_{jk}}{2}\right) \approx \frac{E_a}{E_k}\sin^2\left(\frac{\theta_{aj}}{2}\right) + \frac{E_a}{E_j}\sin^2\left(\frac{\theta_{ak}}{2}\right) \tag{4.2}$$

in the case $i = a$, demonstrating that this condition does not strictly select for double-soft or triple-collinear configurations. We therefore use the same form of the y_{ijk} dimensionless invariants for our initial-state quark pair as is used for final-state particles, to ensure these extra phase-space points outside the triple-collinear or double-soft region are not included.

An important property we expect to see within both A_4^0 as well as its double-soft and triple-collinear limits is that of scale invariance. The parton shower process begins with the central hard collision of two particles; the products of this collision thereafter radiate further bremsstrahlung, and those products themselves can undergo further radiation, such that a self-similar structure arises within these parton showers as you look at increasingly small energy scales. A cutoff must however be placed on this showering process, as the combined Feynman diagram structure relevant to this process at higher energies, modelling the QCD interactions, differ significantly to those modelling the process at lower energies. Ultimately, this creates a fractal structure within the jets of parton showers, and we expect the structure of each sub-jet to be the same, independent of the energy scale at which the jet occurs.

As discussed in Section 2.1.2, the Feynman diagrams for these processes contain virtual propagators, and Section 3.1 demonstrated that the mathematical terms corresponding to these virtual propagators are proportional to

$$\mathcal{M}_{fi} \propto \frac{1}{(p_i + p_j)^2} \equiv \frac{1}{Q^2}, \tag{4.3}$$

where we let Q^2 denote the invariant mass squared of the virtual propagator. Given this, and noting that the Mandelstam variable s is of the same dimensionality as Q^2, we expect certain structure in the terms of A_3^0 and A_4^0. Considering the single-gluon emission antenna function, by definition this involves one particle emission and so we expect terms of order $\mathcal{O}(1/s)$. Similarly, we expect terms of order $\mathcal{O}(1/s^2)$ for the double-gluon emission antenna function, as well as its double-soft and triple-collinear limits. This dimensionality is indeed observed in the form of our antenna functions. In applications of the antenna functions, the Born-level matrix element is multiplied by the corresponding antenna function and then

integrated over the possible momenta. This is demonstrated in Equation 4.4 for the case of double-gluon emission, where we integrate over two momentum scales

$$\int_{Q^2_{\text{low}}}^{Q^2_{\text{high}}} dQ_1^2 dQ_2^2 \cdot |\mathcal{M}_{fi}|^2_{\text{Born}} A_4^0. \tag{4.4}$$

Here we explicitly see that the combined $A_4^0 \cdot dQ_1^2 dQ_2^2$ term will therefore be dimensionless, an expected consequence of the anticipated scale invariance within the structure of parton showers.

For future work, a direct comparison could be undertaken between calculations of $|\mathcal{M}_{fi}|^2_{\text{full}}$ from Equation 3.51 first using current parton shower method, wherein two consecutive single-gluon emission antenna functions are applied to $|\mathcal{M}_{fi}|^2_{\text{Born}}$, and secondly using the initial state A_4^0 given in Appendix 5. This comparison could be executed using the initial-state clustering algorithms of [3], applied to the $q\bar{q} \to Zgg$ configurations generated using the methods described in Section 3.3. Here, we would expect to see explicitly the impact of coherent double-gluon emission, accounted for by the double-gluon emission antenna function A_4^0 that isn't captured by the iterated single-emission functions.

Conclusion

An antenna function for double-gluon emission from a quark-antiquark pair in the initial state was found by applying crossing symmetry to the literature antenna function for double-gluon emission from a quark-antiquark pair in the final state. The double-soft and triple-collinear limits of this antenna function were derived by first substituting λ parameters into the Mandelstam variables and then taking a series expansion about $\lambda = 0$. Both the antenna function and these derived limits demonstrated the expected scale invariance in each of its terms, a result that comes about from the fractal structure of jets created through bremsstrahlung in high-energy particle collisions. Employing a uniform sample over the phase space of this antenna function, enabled by the RAMBO algorithm implemented in *Pythia 8.3*, the antenna function was validated against corresponding matrix element calculations for double-gluon emission evaluated using MadGraph. In a similar fashion, by employing cuts of the phase space around the double-soft and triple-collinear points, these derived limits of the antenna function were also compared against matrix element calculations and were observed to reproduce the limits anticipated from their factorisation. Enabled with the initial state antenna function, the structure of interference effects within double-gluon emissions from quark pairs in the initial state can be further explored, in the context of its relevance for parton shower algorithms.

Bibliography

[1] J. Alwall, M. Herquet, F. Maltoni, O. Mattelaer, and T. Stelzer. Madgraph 5: going beyond. *Journal of High Energy Physics*, 2011(6):128, Jun 2011.

[2] A. Bassetto, M. Ciafaloni, and G. Marchesini. Jet structure and infrared sensitive quantities in perturbative qcd. *Physics Reports*, 100(4):201 – 272, 1983.

[3] A. Daleo, T. Gehrmann, and D. Maître. Antenna subtraction with hadronic initial states. *Journal of High Energy Physics*, 2007(04):016–016, Apr 2007.

[4] R. Kleiss, W. Stirling, and S. Ellis. "A new Monte Carlo treatment of multiparticle phase space at high energies". *Computer Physics Communications*, 40(2):359 – 373, 1986.

[5] A. G.-D. Ridder, T. Gehrmann, and E. N. Glover. Antenna subtraction at NNLO. *Journal of High Energy Physics*, 2005(09):056–056, Sep 2005.

[6] T. Sjöstrand, S. Ask, J. R. Christiansen, R. Corke, N. Desai, P. Ilten, S. Mrenna, S. Prestel, C. O. Rasmussen, and P. Z. Skands. An introduction to PYTHIA 8.2. *Computer Physics Communications*, 191:159–177, Jun 2015.

Appendix

Initial State A_4^0 Antenna Function

$$
\begin{aligned}
A_4^0\left(a_q, b_{\bar{q}}; j_g, k_g\right) = \frac{1}{s_{AB}}\Bigg(& \frac{2s_{ab}^3}{s_{aj}s_{bk}t_{ajk}t_{bjk}} + \frac{2s_{ab}^2}{s_{aj}s_{bk}s_{jk}} + \frac{4s_{ab}^2}{s_{aj}s_{bk}t_{ajk}} - \frac{2s_{ab}^2}{s_{bk}s_{jk}t_{ajk}} + \frac{4s_{ab}^2}{s_{aj}s_{bk}t_{bjk}} - \frac{2s_{ab}^2}{s_{aj}s_{jk}t_{bjk}} \\
& - \frac{4s_{jk}s_{ab}^2}{s_{aj}s_{bk}t_{ajk}t_{bjk}} + \frac{4s_{ab}^2}{s_{aj}t_{ajk}t_{bjk}} + \frac{4s_{ab}^2}{s_{bk}t_{ajk}t_{bjk}} - \frac{8s_{ab}^2}{s_{jk}t_{ajk}t_{bjk}} + \frac{6s_{ab}}{s_{aj}s_{bk}} - \frac{6s_{ab}}{s_{aj}s_{jk}} \\
& - \frac{2s_{ak}s_{ab}}{s_{aj}s_{bk}s_{jk}} - \frac{2s_{bj}s_{ab}}{s_{aj}s_{bk}s_{jk}} - \frac{4s_{ab}}{s_{bk}s_{jk}} - \frac{3s_{jk}s_{ab}}{s_{aj}s_{bk}t_{ajk}} + \frac{6s_{ab}}{s_{aj}t_{ajk}} - \frac{3s_{bj}s_{ab}}{s_{aj}s_{bk}t_{ajk}} + \frac{4s_{ab}}{s_{bk}t_{ajk}} \\
& + \frac{2s_{ak}s_{ab}}{s_{bk}s_{jk}t_{ajk}} + \frac{2s_{bj}s_{ab}}{s_{bk}s_{jk}t_{ajk}} - \frac{8s_{ab}}{s_{jk}t_{ajk}} - \frac{3s_{jk}s_{ab}}{s_{aj}s_{bk}t_{bjk}} + \frac{6s_{ab}}{s_{aj}t_{bjk}} - \frac{3s_{ak}s_{ab}}{s_{aj}s_{bk}t_{bjk}} + \frac{3s_{ab}}{s_{bk}t_{bjk}} \\
& + \frac{2s_{ak}s_{ab}}{s_{aj}s_{jk}t_{bjk}} - \frac{2s_{bk}s_{ab}}{s_{aj}s_{jk}t_{bjk}} - \frac{8s_{ab}}{s_{jk}t_{bjk}} + \frac{3s_{jk}^2s_{ab}}{s_{aj}s_{bk}t_{ajk}t_{bjk}} + \frac{3s_{bk}s_{ab}}{s_{aj}t_{ajk}t_{bjk}} - \frac{6s_{jk}s_{ab}}{s_{aj}t_{ajk}t_{bjk}} \\
& - \frac{3s_{jk}s_{ab}}{s_{bk}t_{ajk}t_{bjk}} - \frac{3s_{ak}s_{ab}}{s_{bk}t_{ajk}t_{bjk}} + \frac{4s_{ak}s_{ab}}{s_{jk}t_{ajk}t_{bjk}} - \frac{4s_{ak}s_{bk}s_{ab}}{s_{jk}^2t_{ajk}t_{bjk}} + \frac{6s_{ab}}{t_{ajk}t_{bjk}} - \frac{s_{jk}s_{ab}}{s_{aj}t_{ajk}^2} + \frac{2s_{ak}^2s_{ab}}{s_{jk}^2t_{ajk}^2} \\
& + \frac{s_{ab}}{t_{ajk}^2} - \frac{s_{jk}s_{ab}}{s_{bk}t_{bjk}^2} - \frac{4s_{bk}s_{ab}}{s_{jk}t_{bjk}^2} + \frac{2s_{bk}^2s_{ab}}{s_{jk}^2t_{bjk}^2} + \frac{3s_{ab}}{t_{bjk}^2} + \frac{2}{s_{aj}} - \frac{3s_{ak}}{s_{aj}s_{bk}} - \frac{3s_{bj}}{s_{aj}s_{bk}} + \frac{2s_{ak}}{s_{aj}s_{jk}} + \frac{4s_{bj}}{s_{aj}s_{jk}} \\
& + \frac{s_{bk}}{s_{aj}s_{jk}} + \frac{s_{ak}^2}{s_{aj}s_{bk}s_{jk}} + \frac{s_{bj}^2}{s_{aj}s_{bk}s_{jk}} + \frac{2s_{aj}}{s_{bk}s_{jk}} + \frac{3s_{ak}}{s_{bk}s_{jk}} - \frac{2}{s_{jk}} + \frac{s_{jk}^2}{s_{aj}s_{bk}t_{ajk}} - \frac{3s_{bj}}{s_{aj}t_{ajk}} \\
& - \frac{s_{bk}}{s_{aj}t_{ajk}} - \frac{2s_{jk}}{s_{aj}t_{ajk}} + \frac{s_{bj}s_{jk}}{s_{aj}s_{bk}t_{ajk}} - \frac{s_{jk}}{s_{bk}t_{ajk}} + \frac{s_{bj}^2}{s_{aj}s_{bk}t_{ajk}} - \frac{s_{ak}}{s_{bk}t_{ajk}} - \frac{s_{bj}}{s_{bk}t_{ajk}} + \frac{2s_{ak}}{s_{jk}t_{ajk}} \\
& + \frac{3s_{bj}}{s_{jk}t_{ajk}} + \frac{s_{bk}}{s_{jk}t_{ajk}} - \frac{s_{ak}^2}{s_{bk}s_{jk}t_{ajk}} - \frac{s_{bj}^2}{s_{bk}s_{jk}t_{ajk}} - \frac{2s_{ak}s_{bj}}{s_{bk}s_{jk}t_{ajk}} + \frac{2s_{ak}^2}{s_{jk}^2t_{ajk}} - \frac{4s_{ak}s_{bk}}{s_{jk}^2t_{ajk}} \\
& + \frac{1}{t_{ajk}} + \frac{s_{jk}^2}{s_{aj}s_{bk}t_{bjk}} - \frac{3s_{ak}}{s_{aj}t_{bjk}} + \frac{3s_{bk}}{s_{aj}t_{bjk}} - \frac{3s_{jk}}{s_{aj}t_{bjk}} + \frac{s_{ak}s_{jk}}{s_{aj}s_{bk}t_{bjk}} + \frac{s_{ak}^2}{s_{aj}s_{bk}t_{bjk}} - \frac{2s_{aj}}{s_{bk}t_{bjk}} \\
& - \frac{2s_{ak}}{s_{bk}t_{bjk}} - \frac{s_{ak}^2}{s_{aj}s_{jk}t_{bjk}} - \frac{s_{bk}^2}{s_{aj}s_{jk}t_{bjk}} + \frac{3s_{aj}}{s_{jk}t_{bjk}} + \frac{5s_{ak}}{s_{jk}t_{bjk}} + \frac{2s_{ak}s_{bk}}{s_{aj}s_{jk}t_{bjk}} - \frac{2s_{bk}}{s_{jk}t_{bjk}} \\
& - \frac{s_{jk}^3}{s_{aj}s_{bk}t_{ajk}t_{bjk}} + \frac{s_{bk}^2}{s_{aj}t_{ajk}t_{bjk}} + \frac{3s_{jk}^2}{s_{aj}t_{ajk}t_{bjk}} + \frac{s_{jk}^2}{s_{bk}t_{ajk}t_{bjk}} - \frac{3s_{ak}}{t_{ajk}t_{bjk}} + \frac{3s_{bk}}{t_{ajk}t_{bjk}} \\
& - \frac{3s_{bk}s_{jk}}{s_{aj}t_{ajk}t_{bjk}} + \frac{s_{ak}s_{jk}}{s_{bk}t_{ajk}t_{bjk}} - \frac{3s_{jk}}{t_{ajk}t_{bjk}} + \frac{s_{ak}^2}{s_{bk}t_{ajk}t_{bjk}} - \frac{2s_{ak}^2}{s_{jk}t_{ajk}t_{bjk}} - \frac{2s_{bk}^2}{s_{jk}t_{ajk}t_{bjk}} \\
& + \frac{4s_{ak}s_{bk}}{s_{jk}t_{ajk}t_{bjk}} + \frac{2s_{bk}^2}{s_{jk}^2t_{bjk}} - \frac{4s_{ak}s_{bk}}{s_{jk}^2t_{bjk}} - \frac{s_{bj}}{t_{ajk}^2} - \frac{s_{bk}}{t_{ajk}^2} + \frac{s_{bj}s_{jk}}{s_{aj}t_{ajk}^2} + \frac{s_{bk}s_{jk}}{s_{aj}t_{ajk}^2} - \frac{2s_{ak}^2s_{bj}}{s_{jk}^2t_{ajk}^2} \\
& - \frac{2s_{ak}^2s_{bk}}{s_{jk}^2t_{ajk}^2} - \frac{3s_{aj}}{t_{bjk}^2} - \frac{3s_{ak}}{t_{bjk}^2} + \frac{s_{aj}s_{jk}}{s_{bk}t_{bjk}^2} + \frac{s_{ak}s_{jk}}{s_{bk}t_{bjk}^2} + \frac{4s_{aj}s_{bk}}{s_{jk}t_{bjk}^2} + \frac{4s_{ak}s_{bk}}{s_{jk}t_{bjk}^2} - \frac{2s_{aj}s_{bk}^2}{s_{jk}^2t_{bjk}^2} - \frac{2s_{ak}s_{bk}^2}{s_{jk}^2t_{bjk}^2}\Bigg)
\end{aligned}
\tag{5.1}
$$